Chirality-assisted spin Hall effect of light in the vicinity of the quasi-antidual symmetry mode of a chiral sphere

R. Ali [*]

Applied Physics Department, Gleb Wataghin Physics Institute, University of Campinas, Campinas 13083-859, São Paulo, Brazil

(Received 25 May 2022; revised 28 October 2022; accepted 30 November 2022; published 16 December 2022; corrected 22 February 2023)

The spin Hall shift (SHS) refers to a transverse shift in the scattering plane during the spin-orbit interaction (SOI). SHS is considerably small when light is scattered by a sphere due to the absence of unidirectional scattering. This work shows that the chiral property of a sphere can offer a platform to optimize the SOI by achieving nearly zero forward scattering with significant backward scattering. As a result, a polarization transformation takes place and the scattered field transfers its maximum spin angular momentum to orbital angular momentum. Consequently, an enhanced transversal shift is observed due to the momentum conservation of the scattered field. The results reveal that the shift strongly depends on the handedness of the chiral sphere and the helicity of the incident beam. Thus, offering an alternative paradigm for the quantitative measurement of chirality parameters of a single chiral nanoparticle. We hope that these results will potentially shed new light on the SOI of various forms that can find potential applications such as optical sensing, chiral resolution of single nanoparticles, precision measurements, and the manipulation of subwavelength nanoparticles.

DOI: 10.1103/PhysRevA.106.063508

I. INTRODUCTION

Light can carry spin angular momentum (SAM) and orbital angular momentum (OAM) due to its intrinsic polarization and spatial (orbital) degrees of freedom [1], respectively. The conversion between the SAM and OAM can be anticipated during the light-matter interaction which emerges from several fascinating phenomenon. For instance, when a circularly polarized (CP) light scatters by a particle it does not propagate in the original plane but it manifests a small transversal spin-dependent shift out of the original plane due to the spin-orbit interaction (SOI) [2–5]. This spin-dependent displacement is a manifestation of the spin-Hall effect of light (SHEL) [6–10], which received significant attention due to its numerous potential applications. In fact, SHEL is actually a photonic counterpart of the Hall effect in electronic systems where the applied electric field and electron spin are replaced with the gradient of the refractive index and polarization of light [11,12]. During the course of SOI, a conversion of SAM to OAM occurs, which is an inevitable and ubiquitous phenomenon appearing when light is scattered by subwavelength particles. Since, during the transformation of SAM to OAM, the total angular momentum is conserved [13], the scattered beam is transversely shifted out of the plane. This spin-dependent shift is the origin of the spin Hall effect of light [10,14–17].

SHS can be exploited for sensing of refractive index of the medium [18], precision measurements like the thickness of thin films [19], the measurement of graphene layers with their conductivity [20,21], and the detection of the rate of chemical reactions [22]. For the usual spherical optical systems, the scattering of light is nearly homogeneous around the particle [23,24], therefore, the scattered field presents weak SOI and results in a small SHS. On the contrary, for planner interfaces such as air-glass and glass-metal interfaces, a large SHS is experimentally demonstrated [19,25–27].

However, several works were presented to optimize the SHS by engineering the optical properties of the sphere. For instance, a large SHS is observed using the plasmonic core-shell [14], topological insulator [17], and by exploiting the duality of a hypothetical magnetic sphere [10]. In this work, we optimize the SOI by achieving the quasi-anti-dual symmetric modes of a spherical particle by introducing the chiral property of the sphere.

Chirality is a geometrical property of an object that shows a lack of mirror symmetry [28] and distinguishable mirror images. These images are commonly known as chiral enantiomers and can further be designated as left- and right-handed chiral enantiomers [28–30]. In this scenario, each enantiomer interacts differently with CP light and performs selective optical phenomena such as scattering, optical rotation, and circular dichroism [31–33]. Recently, we showed that the SOI can be significantly enhanced in the presence of chirality of sphere [30,34,35] or chirality of the surrounding medium [36]. In this perspective, a strong coupling between the chirality parameter κ and incident polarization may lead to a large conversion between SAM to OAM.

Taking inspiration from these findings [30,34,36], one may exploit the SOI between the circularly polarized incident light and subwavelength chiral sphere. In this perspective, we are investigating the chirality-dependent SHS of light by not only the homogeneous chiral sphere, but also for the chiral core-shell particle [28]. We show that an appropriate selection of the chirality parameter and polarization of the incident beam allows harnessing the quasi-anti-dual symmetry of

[*]rali.physicist@gmail.com

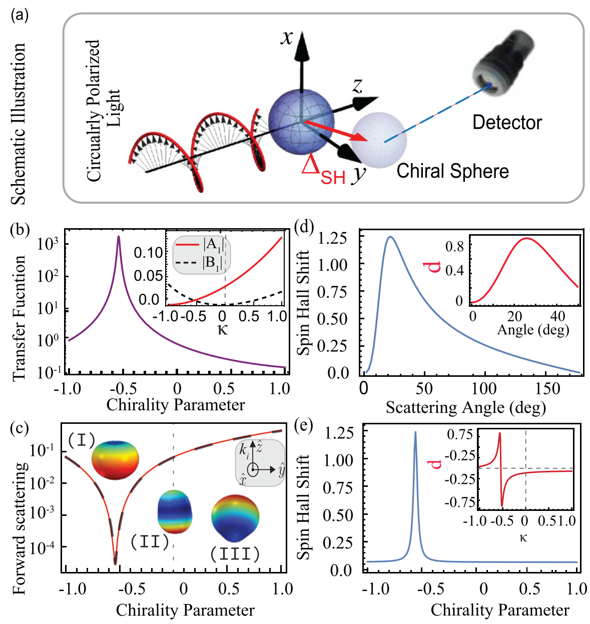

FIG. 1. (a) Schematic illustration of spin Hall shift: a circularly polarized light is impinging on a chiral sphere and corresponding scattered field is observed by a detector. In the view of the detector, the scattered light is emitted by the transversely displaced sphere (indicated by lighter color) instead of the original sphere (indicated by light blue sphere). This apparent transversal shift (indicated by red arrow) in the scattering plane is responsible for SHEL. (b) Transfer function of the particle versus chirality parameter, inset shows the dipolar Mie scattering coefficients. (c) Analytically (solid line) and numerically (COMSOL mulityphysics v5.6) (dashed) calculated forward scattering efficiency vs chirality parameter, insets show numerically calculated 3D sketches: far-field scattering radiation pattern for chirality parameter $\kappa = -0.56$ (I), $\kappa = 0$ (II), and $\kappa = +0.56$ (III). Spin Hall shift (in the unit of wavelength) as a function of (d) scattering angle for fixed $\kappa = -0.56$ and (e) chirality parameter for fixed scattering angle at $\theta = 26^\circ$. Inset of (d,e) represent the diattenuation as a function of scattering angle and chirality parameter, respectively. All of these calculations are carried out by considering left circularly polarized incident light of wavelength 1 μm, radius of the sphere 100 nm, refractive indices of the sphere (medium) $1.58 + \kappa$ ($n_m = 1$).

subwavelength chiral particles. As a result, the chiral particle scatters more momentum in the backward direction and allows us to observe a large spin-dependent SHS.

Since the SHS can be measured experimentally with great success [19,37], it may open an opportunity to characterize the chirality parameter of single plasmonic particles where the traditional methods [30,34–36] cannot be applied.

II. THEORETICAL BACKGROUND

Let us consider a chiral sphere of radius a, refractive index $n_\sigma = \sqrt{\epsilon_p \mu_p} + \sigma\kappa$, where κ is the chirality parameter, $\sigma = 1(-1)$ for left (right) CP light, $\epsilon_p(\mu_p)$ is the relative permittivity (permeability) of the sphere, illuminated by a CP beam as shown in Fig. 1(a). In what follows, we adopt the time-harmonic convention $e^{-i\omega t}$ and ignore the temporal dependence. In this perspective, the light scattered by the chiral sphere can be defined by using the well-established Mie scattering theory [38,39]. Since the impinging field has well-defined helicity, the scattered field by the sphere could have both left- and right-handed CP wave contribution [39]. Thus, it is more convenient to express the scattered electric field $\mathbf{E}_s$ in terms of both-handed scattering modes as [40]

$$\mathbf{E}_s = \sum_{n=|m_z|}^{\infty} i^n (2n+1)^{1/2} \left(\frac{A_n + B_n}{2} \mathbb{A}^{\mathrm{LCP}}_{n,m_z} + \frac{A_n - B_n}{2} \mathbb{A}^{\mathrm{RCP}}_{n,m_z} \right), \tag{1}$$

where A_n and B_n are the effective Mie coefficients for the chiral sphere [34,35], index n denotes the nth-order of spherical harmonics, m_z is the angular momentum projection on the incident laser axis, and $\mathbb{A}^{\mathrm{LCP}}_{n,m_z}$ and $\mathbb{A}^{\mathrm{RCP}}_{n,m_z}$ are the left CP and right CP multipoles [40].

Equation (1) can provide complete information of the polarization state of the scattered light. For instance, the scattered light could have the same (opposite) polarization as of the incident beam if the particle exhibits dual (antidual) symmetric mode [40]. It is worth mentioning that a sphere presents dual (antidual) symmetric mode when the electric A_n and magnetic B_n scattering coefficients of the sphere posses equal magnitude with same (opposite) phases, e.g.. $A_n = B_n$ ($A_n = -B_n$). The dual and antidual symmetry modes in the dielectric sphere can be achieved in quasistatic approximation by considering a particle with $\epsilon_p = \mu_p$ and $\epsilon_p = \frac{4-\mu_p}{2\mu_p+1}$, respectively. Although in the visible frequency range, the naturally occurring materials do not possess a magnetic permeability different than unity $\mu_p \neq 1$, thus making realization of the dual and antidual modes difficult. However, using a high refractive index sphere we can achieve a strong magnetic response due to the rotation of the displacement currents [24,41,42].

To circumvent these limitations, we are exploiting the chirality parameter κ of the sphere as an additional degree of freedom that allows us to achieve antidual symmetric mode. To analyze the duality of the system, we may evaluate the transfer function T which can be written as [40]

$$T = \frac{\sum_n (2n+1)|A_n - B_n|^2}{\sum_n (2n+1)|A_n + B_n|^2}. \tag{2}$$

It defines the ratio between the energy scattered in the backward direction to the energy scattered in the forward direction. It is trivial to note that, in the vicinity of dual mode where the first Kerker's condition is satisfied [23,24,43], the particle should scatter zero energy in the backward direction and $T \to 0$. In contrast, at the antidual mode, where the second Kerker's condition satisfies [24,43], the particle should be scattering zero energy in the forward direction, and in this case, Eq. (2) will lead to $T \to \infty$. For a usual low refractive index sphere, the interference between the electric and magnetic scattering modes is negligibly small and the scattered momentum is nearly homogeneous in all directions. Therefore, the transfer function does not achieve its sharp extremum and hence yield a weak SHS.

The spin Hall shift associated to system illustrated in Fig. 1(a) can be expressed by utilizing the Poynting vector [44] of the scattering field. The transverse spin-dependent shift normal to the scattering plane can be defined as $\Delta_{SH} = \lim_{r\to\infty} r(S_\phi/|S_r|)$, where S_ϕ and $|S_r|$ are the azimuthal and radial components of the scattered Poynting vector. Finally, Δ_{SH} can be expressed by using Mie scattering theory [17] as

$$\Delta_{SH} = \frac{\sigma \sin\theta}{k} \frac{\mathrm{Re}\left[\sum_{n=1}(2n+1)(S_1^* \cdot A_n\pi_n + S_2 \cdot (B_n\pi_n)^*)\right]}{|S_1|^2 + |S_2|^2}, \tag{3}$$

where S_1 and S_2 are the scattering matrix amplitudes [38]

$$S_1 = \sum_n \frac{2n+1}{n(n+1)}[A_n\pi_n(\cos\theta) + B_n\tau_n(\cos\theta)], \tag{4}$$

$$S_2 = \sum_n \frac{2n+1}{n(n+1)}[A_n\tau_n(\cos\theta) + B_n\pi_n(\cos\theta)]. \tag{5}$$

Here, $\pi_n(\cos\theta)$ and $\tau_n(\cos\theta)$ are the angle-dependent functions.

Analytical analysis of the enhanced SHS

For the long wavelength regime, where only dipolar modes are excited, one can simplify the angle-dependent functions as $\tau_1(\cos\theta) = \cos\theta$ and $\pi_1(\cos\theta) = 1$. Now Eqs. (4) and (5) can be expressed as

$$S_1 = 3/2(A_1 + B_1\cos\theta), \quad S_2 = 3/2(A_1\cos\theta + B_1),$$

respectively. It is interesting to note that, in the vicinity of dual ($A_1 \approx B_1$) and antidual ($A_1 \approx -B_1$) modes of the chiral particle, both S_1 and S_2 approach zero simultaneously at $\theta = 180^\circ$ and $\theta = 0^\circ$, respectively. Thus, Eq. (3) suggests that both dual and antidual modes should lead to an enhanced SHS. It is worth mentioning that dual and antidual symmetric modes can appear for $\mu_p \neq 1$, which is rather difficult for the nonmagnetic low refractive index sphere. In this perspective, this work utilizes the sphere chirality parameter κ to achieve nearly identical scattering amplitudes $A_1 \approx -B_1$ and hereinafter we will call them as the quasi-anti-dual symmetric modes. In the vicinity of the quasi-anti-dual symmetric mode of the system. The sphere will scatter light in the backward direction with nearly zero forward scattering. Thus a large SHS is expected to occur.

III. RESULTS AND DISCUSSION

In the following discussion we consider a circularly polarized plane wave of vacuum wavelength $\lambda_0 = 1\,\mu\mathrm{m}$, scattering by a chiral sphere of radius $a = 100\,\mathrm{nm}$, relative permittivity (permeability) $\epsilon_p = 2.5 (\mu_p = 1)$ immersed in an aqueous solution of refractive index n_m. Without going into the detail and specification of chiral materials, for the sake of broader readership we generalize our findings by taking chirality parameter κ ranging from -1 to $+1$. This range of chirality parameter was already used by several well-reputed research groups [45–50].

To elucidate the role of the chirality parameter on the duality symmetry of the system, we calculate the transfer function T versus the chirality parameter in Fig. 1(b). It is shown that at chirality parameter $\kappa = -0.56$, T attains its maximum value $T \to 10^3$, which means the particle is scattering more optical momentum in the backward direction. Equation (2) suggests that the sharp peak of T appears due to the occurrence of the quasi-anti-dual symmetric mode ($A_1 \approx -B_1$). For the concreteness of this fact, we estimate the absolute values of the dipolar scattering amplitudes $|A_1|$ and $|B_1|$ in the inset of Fig. 1(b) and they appear identical at $\kappa = -0.56$ as expected.

To see the directional scattering profile close to the antidual symmetric mode, we calculate the forward-scattering efficiency (Q_f) (an explicit expression of Q_f is given in Appendix A) in Fig. 1(c) as a function of κ. It is shown that Q_f is substantially suppressed at $\kappa = -0.56$ which appears due to the destructive interference between the electric and magnetic scattering amplitudes. To obtain more insight, we numerically (COMSOL Multiphysics) calculate three-dimensional (3D) sketches of far-field radiation pattern and shown in the insets of the Fig. 1(c) for the different chirality parameter: (I) $\kappa = -0.56$, (II) $\kappa = 0$, and (III) $\kappa = 0.56$. It is shown that the sphere with quasi-anti-dual symmetric mode scatters zero momentum in the forward direction (I) and the sphere with $\kappa = 0$ behaves like a typical dipole scatterer (II). In contrast, the left-handed chiral sphere scatters large momentum in the forward direction (III). As a result, a large transfer function is only achieved at quasi-anti-dual symmetric mode, e.g., at $\kappa = -0.56$. It is important to mention that, close to the quasi-anti-dual mode the denominator of Eq. (3) $|S_1|^2 + |S_2|^2$ should be minimum and hence Eq. (3) predicts a large spin Hall shift.

In Fig. 1(d), we plot Δ_{SH} (in units of λ) as a function of the scattering angle for a fixed chirality parameter at $\kappa = -0.56$. It is demonstrated that a large SHS appears at $\theta = 26^\circ$ as expected. In addition to this analytical approach, the enhanced SHS can be understood by analyzing the conversion of SAM to OAM. In fact, during this conversion the total angular momentum of the scattered field is conserved, as a result, the scattering plane has to be shifted out of the original plane by Δ_{SH}. For this particular configuration, a large shift appears at $\theta = 26^\circ$ [see Fig. 1(c)], which implies that the maximum SAM converts to OAM at $\theta = 26^\circ$.

To elucidate the transformation of SAM to OAM, we can analyze the differential attenuation of the orthogonal polarization state such as the diattenuation function $d(\theta)$, which can be defined as

$$d(\theta) = \frac{|S_2|^2\cos^2\theta - |S_1|^2}{|S_2|^2\cos^2\theta + |S_1|^2}. \tag{6}$$

During the course of the light-matter interaction when no SAM to OAM transformation occurs, $d(\theta) = 0$ is measured. In contrast, a complete SAM-to-OAM conversion gives $d(\theta) = 1$. To evaluate the role of SAM-to-OAM conversion on SHS, we calculate $d(\theta)$ versus θ in the inset of Fig. 1(d) for fixed $\kappa = -0.56$. It is clearly shown that $d(\theta)$ approaches its maximum value $d(26^\circ) \approx 0.96$ at $\theta = 26^\circ$. Thus, the scattered field has maximally transferred its SAM. This nearly complete transformation of SAM to OAM is responsible for the enhancement of Δ_{SH}.

To demonstrate the role of other values of the chirality parameter, in Fig. 1(e) we plot Δ_{SH} as a function of κ for fixed scattering angle $\theta = 26^\circ$. The results indicate that a left CP light strongly interacts with right-handed chiral particles and due to the strong SOI, maximum SAM is converted to OAM. Thus, a large SHS is found at $\kappa = -0.56$. On the same footing, in the inset of Fig. 1(e) we calculate the $d(\theta)$ as a function of the chirality parameter for fixed $\theta = 26^\circ$, the

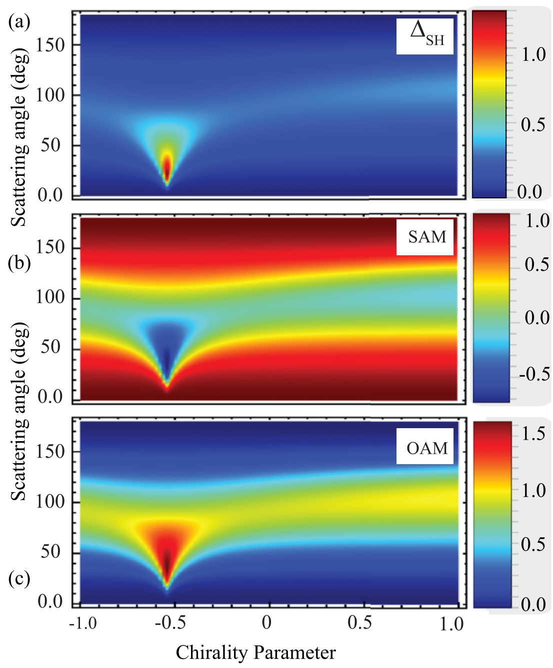

FIG. 2. (a) Color map of the normalized spin Hall shift Δ_{SH} (in units of wavelength) versus chirality parameter and the scattering angle. The maximum enhancement at $\kappa = -0.56$ is clearly observed. Distributions of (b) spin angular momentum and (c) orbital angular momentum per photon as a function of chirality parameter and scattering angle. The colorscale illustrates the values of OAM per photon that exceed the incident AM per photon which can be related to the negative spin density values. Since the total momentum per scattered photon is conserved, the corresponding colorscale in all region satisfies the relation $\ell_s + s_z = 1$.

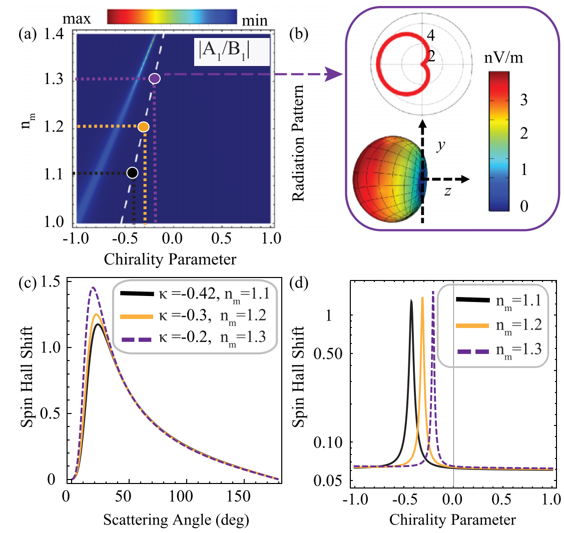

FIG. 3. Panel (a) illustrates a ratio between electric A_1 and magnetic B_1 chiral dipoles as a function of chiral parameter and refractive index of the surrounding medium n_m, where white dashed line indicates the parameter space corresponding to $A_1/B_1 = 1$. (b) Numerically calculated polar plot and 3D sketch of Far-field radiation pattern, z axis shows the direction of incident beam. Δ_{SH} in units of wavelength is calculated as a function of (c) scattering angles and (d) chirality parameter. Here, all other parameters are the same as taken in Figs. 1 and 2.

sharp decay of $d(\theta)$ at $\kappa = -0.56$ is also evidence of the polarization transformation.

The origin of SHS can also be understood by revisiting the SAM and OAM per photon in the far-field scattering regime. For the system sketched in Fig. 1(a), the contribution of SAM and OAM per photon can be written as [51,52]

$$s_z = -i\frac{\left(\mathbf{E}_\sigma^{\mathrm{scat}*} \times \mathbf{E}_\sigma^{\mathrm{scat}}\right)\hat{z}}{\mathbf{E}_\sigma^{\mathrm{scat}*}\mathbf{E}_\sigma^{\mathrm{scat}}}, \tag{7}$$

and

$$\ell_z = -i\frac{\left[\mathbf{E}_\sigma^{\mathrm{scat}*} \times (L_z\mathbf{E}_\sigma^{\mathrm{scat}})\right]\hat{z}}{\mathbf{E}_\sigma^{\mathrm{scat}*}\mathbf{E}_\sigma^{\mathrm{scat}}}, \tag{8}$$

respectively, where $L_z = -i(\mathbf{r} \times \nabla)_z$ is the OAM operator. Since the total angular momentum of the incident field is preserved and the scattered plane wave which involves only $m_z = \sigma$, would be an eigenfunction of the z component of the total angular momentum operator $\mathbf{J}$ with eigenvalue j_z. Thus, the total angular momentum density per photon of the scattered field should also be conserved such that $j_z = \ell_z + s_z$.

To gain further insight into the conditions required for the large SHS, in Fig. 2(a) we demonstrate the apparent SHS [associated with the scattering problem sketched in Fig. 1(a)] versus chirality parameter and scattering angle. It can be seen that for all the parameter space, Δ_{SH} has only one maxima appearing due to the antidual nature of the chiral sphere at $\kappa = -0.56$, as shown in Fig. 1(b). To establish the connection between SHS with optical momentum conversion, next we calculate s_z and ℓ_z in Figs. 2(b) and 2(c), respectively. It is important to emphasize that the sum of the total angular momentum per photon should be conserved and equal to the helicity of the incident beam. Equation (7) suggests that SAM per photon varies $-1 < s_z < 1$ and Fig. 2(b) shows that the scattered photon carries negative spin density ($s_z \sim -0.6$) when SHS is enhanced. Therefore, OAM per scattered photon should have to acquire a large value $\ell_z = 1.6$ than the incident angular momentum $j_z = 1$ to conserve the total angular momentum. This phenomenon was previously referred to as *supermomentum* with an extreme value of $\ell_z = 2\sigma$ [53,54]. It is worth emphasizing that the scattered light can posses $\ell_z = 2\sigma$ when particle scatters exactly zero forward scattering, where the asymmetry parameter (g) [38] has to reach at $g = -1/2$ (see Sec. 1 B). Since for a passive sphere $g > -1/2$ due to the limitation imposed by the optical theorem [55], $\ell_z < 2$ and $0 > s_z > -1$. In the all scenarios, the total angular momentum per photon after scattering is conserved $\ell_z + s_z = \sigma = 1$ for all κ and θ, the enhanced SHS is only found when maximum SAM is converted to OAM.

It is worth mentioning that the enhancement of SHS does not require the large value of the chirality parameter that we used in the previous discussion. However, it can be varied along the chirality axis by changing the material parameters and other length scales involved in the scattering problem. With this perspective, we analyze the effect of the surrounding medium to tune the position of SHS toward the lower value of the chirality parameter. To this end, in Fig. 3(a) we calculate $|A_1/B_1|$ as a function of chirality parameter and medium refractive index n_m to estimate the required values of κ and n_m to achieve the quasi-anti-dual symmetric mode. The white dashed line in Fig. 3(a) indicates where the condition $|A_1/B_1| = 1$ satisfies and the particle exhibits quasi-anti-dual mode with nearly zero forward scattering. To unveil the effect of n_m on SHS, we marked three different points as highlighted by the circles and the corresponding parameters like κ and n_m are indicated by the dotted lines. To see the scattering profile at the circles, we numerically calculate the polar sketches of the far-field radiation pattern using COMSOL, and shown in Fig. 3(b). It is confirmed that along the white dashed line the second Kerker's condition is satisfied. Further details can be found in the Appendix.

Figure 3(c) represents SHS (in units of the wavelength) versus scattering angle for different chirality parameters and medium refractive as mentioned in the inset. The results show that an enhancement of Δ_{SH} is found close to the $\theta = 20^\circ$, where the maximum conversion of SAM to OAM occurs due to the antidual symmetric mode. In Fig. 3(c) we present Δ_{SH} as a function of chirality parameter for fixed scattering angle at $\theta = 20^\circ$ for different n_m as indicated in the inset. It is clearly shown that with the increase in the medium's refractive index the peak of Δ_{SH} is shifted to a lower chirality parameter, whereas the SHS on the opposite-handed chiral sphere (in this case, the left-handed chiral sphere $\kappa > 0$) does not show much variation. Thus, altogether this platform provides a strategy to sense the chirality of a single nanoparticle on the basis of the enhanced spin Hall shift. To see the Δ_{SH} on the opposite-handed chiral sphere we may revert the incident polarization which will lead to negative Δ_{SH} on the chiral sphere.

For the concreteness of this chiral enantioselection based on the SHS technique, let us extend this idea to measure the chirality parameter of chiral core-shell particles. For the sake of generality we consider the dielectric core and chiral shell. The chiral core-shell particles may constitute a variety of chiral structures such as an achiral (dielectric or metallic) core coated with chiral materials [56–60] or an achiral core decorated with achiral metallic nanoparticles forming a plasmonic raspberry-like core-shell structure [28,31,61–63]. In the first case, the chiral response appears due to the chiral shell, while in the second case (where metallic particles are randomly oriented over the achiral core) the chiral response may appear due to the random orientation of the metallic particles. It is due to the fact that the random structures are chiral and show large natural optical activity [64], thus they ultimately govern the optical chiral response [64–66].

However, the handedness and geometrical chirality of many of these artificial plasmonic structures are not *a priori* known after the nanofabrication process. In addition, many applications utilize single isolated plasmonic raspberry-like structures with unknown handedness and unique optical properties. In these cases, traditional probes of chirality, such as rotatory power and circular dichroism are expected to fail to measure the chiroptical properties of the single particle as they typically provide an average chiral response of these structures in solution.

For this configuration, we consider a polystyrene core of radius b, refractive index $n_c = \sqrt{\epsilon_c}$ coated with a chiral shell of thickness t, refractive index $n_s = \sqrt{\epsilon_s} + \sigma\kappa$, where ϵ_c and ϵ_s are the permittivity of the core and shell, respectively. For

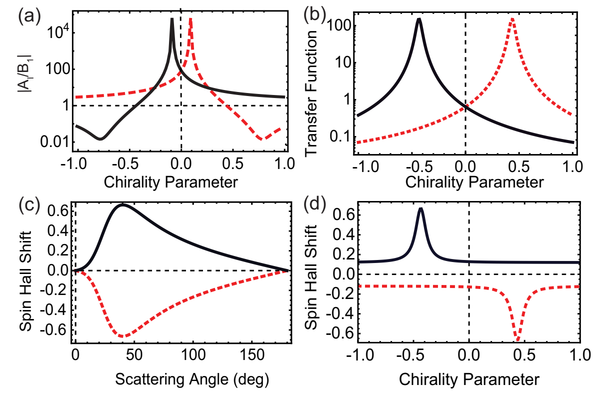

FIG. 4. (a) Plot of $|A_1/B_1|$ as function of chirality parameter for chiral core shell, where the horizontal dashed line indicates $|A_1/B_1| = 1$. (b) Transfer function versus chirality parameter for left (black) and right (dotted) circularly polarized incident beam. (c) SHS for fixed $\kappa = -0.44$ $(+0.44)$ as a function of scattering angle and (d) SHS for fixed scattering angle at $\theta = 41^\circ$ as a function chirality parameter for $\sigma = +1$ $(\sigma = -1)$ indicated by black (dotted).

the numerical calculation presented in Fig. 4, we consider the relative permittivity of the core (shell) $\epsilon_c = 2.5$ $(n_s = 2.89 + 0.05i)$, radius of the core $b = 60$ nm, and shell thickness $t = 40$ nm. Since the particle has an imaginary refractive index, therefore, our previous enantioselective methods [30,34–36] may not be applied to detect the chiral handedness of the sphere.

To estimate the required chirality parameter to achieve the quasi-anti-dual condition for this particular configuration, in Fig. 4(a), we calculate $|A_1/B_1|$ of the core-shell particle as a function of κ for different polarization. The explicit expressions of A_n and B_n for the core-shell particle can be found in Ref. [30]. Note that the chiroptical response is symmetric when we change the polarization as illustrated in Fig. 4(a). It is clear that $|A_1| \approx |B_1|$ at $\kappa = -0.44$ $(\kappa = 0.44)$ for the right (left) CP incidence as marked by intersection points of the horizontal dashed line. Thus, the quasi-anti-dual symmetric mode is achieved and the core-shell nanoparticle scatters more energy in the backward direction. Hence, the transfer function should be maximum as shown in Fig. 4(b), where the transfer function is plotted versus the chirality parameter.

In fact, the forward scattering by the chiral core-shell particle is suppressed at $\kappa = -0.44$ and there must be a polarization transition between the forward and backward scattering, which ultimately leads to a strong SOI at particular scattering angle. In Fig. 4(c), we calculate the SHS versus scattering angle and the results show that the large shift appears between $\theta = 25^\circ$ to 60°. Finally, in Fig. 4(d) we fix the scattering angle at $\theta = 40^\circ$ to calculate the Δ_{SH} as a function of the chirality parameter. It is indicated that only the right-handed chiral sphere with $\kappa = -0.44$ undergoes a large SHS while the SHS for the left-handed particle is very small. Thus, we can detect the nature of the chirality parameter of a single nanoparticle. However, the spin Hall shift on the left-handed chiral sphere can be achieved by reversing the polarization of the incident light beam. For this case, we also present a parallel calculation for the left CP $(\sigma = -1)$ incident field and the enhanced shift is found at $\kappa = 0.44$.

IV. CONCLUSION

In summary, we investigated the SHEL for the chiral sphere in the vicinity of quasi-anti-dual symmetry. It was shown that an appropriate combination of chirality and other material parameters involved in the scattering problem allows us to equally excite the electric and magnetic chiral dipoles to perform destructive interference in the forward direction. As a result, chiral particle scatters more energy in the backward direction. This phenomenon reveals a polarization transformation of the scattered field and optimizes the spin-orbit interaction. As a result, the all spin angular momentum of the beam is converted to orbital angular momentum and the scattered field only carries orbital angular momentum. To this end, the incident light transfers its all SAM to OAM. Consequently, this complete conversion of the optical momentum leads to an optimal shift in the scattered light by the sphere. By considering two different examples such as a homogeneous chiral sphere and chiral core-shell, we showed that the chirality-dependent SHS can be exploited to detect the chiral nature of a single plasmonic chiral nanosphere, where traditional methods may not be applied. Hence, we expect that the large SHEL should be detected in experiments and plays significant roles in the analysis of optical chiral sensing particularly *to characterize the chirality of a single particle* and potential applications in precision metrology.

ACKNOWLEDGMENTS

We thank G. Wiederhecker, T. P. M. Alegre, F. A. Pinheiro and P. A. M. Neto for inspiring discussion. This work is supported by Fundacão de Amparo a Pesquisa do Estado de São Paulo (FAPESP) through Project No. 2020/03131-2.

The author declares no conflicts of interest.

APPENDIX A: MIE SCATTERING BY CHIRAL SPHERE

This Appendix contains an expanded theoretical description of light scattering by a chiral particle and orbital angular momentum per photon of the scattered light, where explicit expressions of the directional scattering (e.g., forward scattering and backward scattering), SOM and OAM are presented. Furthermore, we also briefly described the COMSOL multiphysics implementation for a chiral sphere.

Electromagnetic field in chiral media

Let us consider an electromagnetic incident field $\mathbf{E}_{\text{inc}}$ illuminating a chiral sphere of radius a immersed in a nonmagnetic dielectric host medium. By following the Bohren decomposition method [38], we express the electromagnetic field in terms of the linear combinations of the vector wave function in spherical coordinates as

$$\mathbf{E}_{\text{in}} = E_0 \sum_{\ell=1}^{\infty} i^{\ell} \frac{2\ell+1}{\ell(\ell+1)} \big(M^{(1)}_{o1\ell} - iN^{(1)}_{e1\ell}\big), \tag{A1}$$

$$\mathbf{H}_{\text{in}} = H_0 \sum_{\ell=1}^{\infty} i^{\ell} \frac{2\ell+1}{\ell(\ell+1)} \big(M^{(1)}_{e1\ell} + iN^{(1)}_{o1\ell}\big), \tag{A2}$$

where $M_{e1\ell}$, $M_{o1\ell}$, $N_{e1\ell}$, and $N_{o1\ell}$ are the vector spherical harmonics [39] and $H_0 = \frac{k}{\omega\mu}E_0$. Since the electric $\mathbf{E}$ and magnetic $\mathbf{H}$ fields inside the chiral sphere are coupled by a phonological constant κ. Therefore, it can be described by the following modified constitutive relations

$$\begin{aligned} \mathbf{D} &= \epsilon_0\epsilon_p \mathbf{E} + i\kappa\sqrt{\epsilon_0\mu_0}\,\mathbf{H}, \\ \mathbf{B} &= -i\kappa\sqrt{\epsilon_0\mu_0}\,\mathbf{E} + \mu_p\mu_0\mathbf{H}, \end{aligned} \tag{A3}$$

where $\mathbf{D}$ and $\mathbf{B}$ are the electric displacement and the magnetic field, respectively. Furthermore, ϵ_0 (μ_0) is the vacuum permittivity (permeability). By using these constitutive relations in the Maxwell's equations for chiral media in the frequency domain, the coupling between the $\mathbf{E}$ and $\mathbf{H}$ can be removed through the linear transformation [36,39]. Finally, a straightforward calculation allows us to define the scattered field by the chiral sphere in the surrounding medium as [39]

$$\begin{aligned} \mathbf{E}_s &= E_0 \sum_{\ell}^{\infty} (i)^{\ell} \frac{2\ell+1}{\ell(\ell+1)} \\ &\quad \times \big(ia_\ell N^3_{e1\ell} - b_\ell M^3_{o1\ell} + c_\ell M^3_{e1\ell} - id_\ell N^3_{o1\ell}\big), \\ \mathbf{H}_s &= H_0 \sum_{\ell}^{\infty} (i)^{\ell} \frac{2\ell+1}{\ell(\ell+1)} \\ &\quad \times \big(a_\ell M^3_{e1\ell} + ib_\ell N^3_{o1\ell} - ic_\ell N^3_{e1\ell} - d_\ell M^3_{o1\ell}\big), \end{aligned} \tag{A4}$$

where a_ℓ, b_ℓ, c_ℓ, and d_ℓ are commonly known as Mie coefficients that can be calculated using a subsidiary boundary condition at the sphere surface and defined as

$$\begin{aligned} a_\ell &= \frac{V_\ell(-)A_\ell(+) + V_\ell(+)A_\ell(-)}{W_\ell(+)V_\ell(-) + V_\ell(+)W_\ell(-)}, \\ b_\ell &= \frac{W_\ell(+)B_\ell(-) + W_\ell(-)B_\ell(+)}{W_\ell(+)V_\ell(-) + V_\ell(+)W_\ell(-)}, \\ c_\ell &= -d_\ell = i\frac{W_\ell(-)A_\ell(+) - W_\ell(+)A_\ell(-)}{W_\ell(+)V_\ell(-) + V_\ell(+)W_\ell(-)}, \end{aligned} \tag{A5}$$

with

$$\begin{aligned} W_\ell(\sigma) &= m\psi_\ell(y_\sigma)\xi'_\ell(x) - \xi_\ell(x)\psi'_\ell(y_\sigma), \\ V_\ell(\sigma) &= \psi_\ell(y_\sigma)\xi'_\ell(x) - m\xi_\ell(x)\psi'_\ell(y_\sigma), \\ A_\ell(\sigma) &= m\psi_\ell(y_\sigma)\psi'_\ell(x) - \psi_\ell(x)\psi'_\ell(y_\sigma), \\ B_\ell(\sigma) &= \psi_\ell(y_\sigma)\psi'_\ell(x) - m\psi_\ell(x)\psi'_\ell(y_\sigma), \end{aligned} \tag{A6}$$

where $m = m_+m_-/2(m_+ + m_-)$. The Riccati-Bessel functions ψ_ℓ, ξ_ℓ are evaluated either at the size parameter $x = \sqrt{\epsilon_w}k_0a$ defined with respect to the wavelength in the nonmagnetic achiral host medium (relative electric permittivity ϵ_w) or at $y_\sigma = m_\sigma x/\sqrt{\epsilon_w}$. For the sake of convenec we can define the effective scattering coefficients $A_\ell = a_\ell + i\sigma c_\ell$ and $B_\ell = b_\ell - i\sigma d_\ell$ for circularly polarized light of helicity σ [30,34].

To explore the role of the chirality parameter on the transfer function and directional scattering, let us consider further detail of the scattering properties of a small chiral sphere $a \ll \lambda$, where only the dipole scattered fields are excited. In this domain, the induced dipole moments become proportional to the external fields, and is usually written in terms of the particle's electric, magnetic and chiral polarizabilities α_{ee}, α_{mm}, and α_{em},

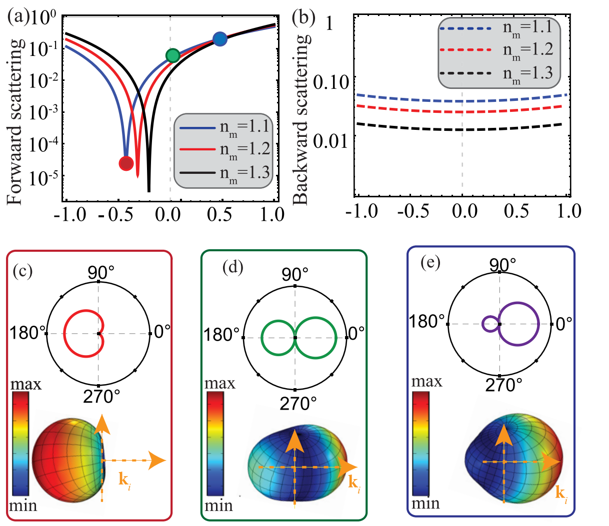

FIG. 5. (a) Forward scattering efficiency Q_f and (b) backward scattering efficiency Q_b as a function of chirality parameter for different medium refractive index. This scattering profile corresponds to Fig. 3 of the main text. Numerically calculated radiation pattern at the dots on blue line of (a). This figure shows that Q_f strongly depends in κ and one can achieve zero forward scattering by exploiting chirality parameter.

respectively,

$$\begin{aligned} a_1 &= \frac{k_0^3}{i6\pi\epsilon_0}\alpha, \quad b_1 = \frac{k_0^3\mu_0}{i6\pi}\alpha_{mm},\\ c_1 &= \frac{k_0^3\sqrt{\mu_0}}{6\pi\sqrt{\epsilon_0}}\alpha_{em}, \quad d_1 = -\frac{k_0^3\sqrt{\mu_0}}{6\pi\sqrt{\epsilon_0}}\alpha_{em}. \end{aligned} \tag{A7}$$

The explicit expressions for the polarizabilities can be manifested by a Taylor expansion with leading-order terms x^3 and we get the generalization of the Clausius-Mossotti relations for a chiral particle as

$$\begin{aligned} \alpha_{ee} &= 4\pi a^3 \frac{3\epsilon_s - 3 - \kappa^2}{3\epsilon_s + 6 - \kappa^2},\\ \alpha_{mm} &= 4\pi a^3 \frac{\kappa^2}{3\epsilon_s + 6 - \kappa^2},\\ \alpha_{em} &= 12\pi a^3 \frac{\kappa}{3\epsilon_s + 6 - \kappa^2}. \end{aligned} \tag{A8}$$

By using the definition of the scattering dipoles, the scattering of light in the forward direction and in the backward direction can be written in terms of the polarizabilities [24,38] as

$$\begin{aligned} Q_f &= \frac{3}{x^2}(A_1 + B_1) \propto \frac{1}{x^2}(\alpha_{ee} + \alpha_{mm} + 2i\alpha_{em}),\\ Q_b &= \frac{3}{x^2}(A_1 - B_1) \propto \frac{1}{x^2}(\alpha_{ee} - \alpha_{mm}). \end{aligned} \tag{A9}$$

Equation (A8) shows that α_{ee} and α_{mm} are even in κ and α_{em} is odd in κ. Thus, from Eq. (A9) it is clear that the forward scattering strongly depends on the chiral parameter while backward scattering does not. For numerical demonstration of this fact, in Fig. 5 we demonstrate [Fig. 5(a)] forward scattering and [Fig. 5(b)] backward scattering as a function of the chirality parameter for the different refractive index of the surrounding medium n_m. It was shown that the forward scattering by the right-handed chiral sphere immersed in a medium with refractive index n_m: 1.1 (blue), 1.2 (red), and 1.3 (black) is strongly reduced at $\kappa = -0.42$ (blue), $\kappa = -0.31$ (red), and $\kappa = -0.2$ (black), respectively. Whereas, the backward scattering does not show a considerable variation along the chirality axis.

Figuress 5(e) and 5(d) present the numerically calculated far-field radiation polar plots and their 3D sketches for the chiral sphere immersed in a medium with refractive index $n_m = 1.1$ for different chirality parameter [Fig. 5(c)] $\kappa = -0.42$, [Fig. 5(d)] $\kappa = 0$, and [Fig. 5(e)] $\kappa = 0.42$. The results show that it is possible to achieve the zero forward scattering by selecting an appropriate combination of the material parameters and other lengthscales involved in the scattering problem.

APPENDIX B: ORBITAL ANGULAR MOMENTUM

The system under consideration exhibits axial symmetry around the beam axis, where the total angular momentum of the incident beam is preserved and equal to the helicity of the incident beam σ. Furthermore, the scattered field, which can only involve $m = \sigma$, is an eigenfunction of the z component of the total angular momentum operator $\mathbf{J}$ with eigenvalue j_z, such that

$$j_z = \frac{\mathbf{E}_\sigma^{\text{scat}*}(\mathbf{L}_z + \mathbf{S}_z)\mathbf{E}_\sigma^{\text{scat}}}{\mathbf{E}_\sigma^{\text{scat}*}\mathbf{E}_\sigma^{\text{scat}}} = \ell_z + s_z = \sigma, \tag{B1}$$

where ℓ_z and s_z are given as in Eqs. (8) and (7), respectively, of the main text. In the case of long wavelength regime, where only the chiral dipolar is excited, the conservation of momentum leads us to the study of the exchange between the SAM and OAM contributions per photon that can be expressed by analyzing the following relation regime:

$$\ell_z = \frac{\sigma \sin^2\theta(1 + 2g\cos\theta)}{1 + \cos^2\theta + 4g\cos\theta}, \tag{B2}$$

$$s_z = \frac{2\sigma\cos\theta(1 + \cos^2\theta)g + \cos\theta}{1 + \cos^2\theta + 4g\cos\theta}, \tag{B3}$$

$$g = \frac{\int_\Omega \frac{dQ_s}{d\Omega}\cos\theta d\Omega}{\int_\Omega \frac{dQ_s}{d\Omega} d\Omega} = \frac{Re(A_1 B_1^*)}{|A_1|^2 + |B_1|^2}, \tag{B4}$$

where g is the asymmetric parameter that defines in terms of the average cosine of all scattering angles.

Equation (B4) suggests that the OAM of the scattered light can reach its extreme value $\ell_z = 2\sigma$ when the particle presents exactly dual symmetric modes with $A_1 = -B_1$. At this condition, the asymmetric parameter reaches $g = -1/2$ as predicted by Eq. (B4). Since the sphere is passive due to the limitations imposed by the optical theorem $g > -1/2$ and $\ell_z = 1.6$ is measured as shown in Fig. 2.

APPENDIX C: COMSOL SIMULATION OF CHIRAL SPHERE

Numerical simulation of the chiral Mie scattering is carried out by using COMSOL Multiphysics software v5.6. Since for chiral materials the electric displacement vector and magnetic induction vector are different that ordinary isotropic dielectric materials are defined as in Eq. (A3). Therefore, constitutive relations within COMSOL were modified to solves Maxwell's equations. Here we adopted the following modifications to the wave optics module, electromagnetic waves frequency domain that were implemented in several works [67,68].

The equation for **D** is modified as (here we use κ = kappa mu0_const. = μ_0, ϵ0_const. = ϵ_0),

$$\begin{aligned}\mathbf{emw.Dx} &\rightarrow \epsilon0\_\text{const.} * emw.Ex + emw.Px - i/c\_\text{const.} * \kappa * emw.Hx,\\ \mathbf{emw.Dy} &\rightarrow \epsilon0\_\text{const.} * emw.Ey + emw.Py - i/c\_\text{const.} * \kappa * emw.Hy,\\ \mathbf{emw.Dz} &\rightarrow \epsilon0\_\text{const.} * emw.Ez + emw.Pz - i/c\_\text{const.} * \kappa * emw.Hz.\end{aligned} \tag{C1}$$

The equation for **H** components is modified as

$$\begin{aligned}\mathbf{emw.Hx} \rightarrow\ & (emw.murinvxx * emw.Bx + emw.murinvxy * emw.By + emw.murinvxz * emw.Bz - i/c\_const * kappa *\\ & \times [emw.murinvxx * emw.Ex + emw.murinvxy * emw.Ey + emw.murinvxz * emw.Ez)]/mu0\_const\\ \mathbf{emw.Hy} \rightarrow\ & (emw.murinvyx * emw.Bx + emw.murinvyy * emw.By + emw.murinvyz * emw.Bz - i/c\_const * kappa *\\ & \times [emw.murinvyx * emw.Ex + emw.murinvyy * emw.Ey + emw.murinvyz * emw.Ez)]/mu0\_const\\ \mathbf{emw.Hz} \rightarrow\ & (emw.murinvzx * emw.Bx + emw.murinvzy * emw.By + emw.murinvzz * emw.Bz - i/c\_const * kappa *\\ & \times [emw.murinvzx * emw.Ex + emw.murinvzy * emw.Ey + emw.murinvzz * emw.Ez)]/mu0\_const\end{aligned} \tag{C2}$$

The equation for dH/dt components is modified as

$$\begin{aligned}\mathbf{emw.dHdtx} \rightarrow\ & (emw.murinvxx * emw.dBdtx + emw.murinvxy * emw.dBdty + emw.murinvxz * emw.dBdtz\\ & + emw.\omega/c\_\text{const.} * \kappa * [emw.murinvxx * emw.Ex\\ & + emw.murinvxy * emw.Ey + emw.murinvxz * emw.Ez)]/mu0\_\text{const.},\\ \mathbf{emw.dHdty} \rightarrow\ & (emw.murinvyx * emw.dBdtx + emw.murinvyy * emw.dBdty + emw.murinvyz * emw.dBdtz +\\ & \times\ emw.\omega/c\_\text{const.} * \kappa * [emw.murinvyx * emw.Ex + emw.murinvyy * emw.Ey\\ & + emw.murinvyz * emw.Ez)]/mu0\_\text{const.},\\ \mathbf{emw.dHdtz} \rightarrow\ & (emw.murinvzx * emw.dBdtx + emw.murinvzy * emw.dBdty + emw.murinvzz * emw.dBdtz\\ & + emw.\omega/c\_\text{const.} * \kappa * [emw.murinvzx * emw.Ex\\ & + emw.murinvzy * emw.Ey + emw.murinvzz * emw.Ez)]/mu0\_\text{const.}\end{aligned} \tag{C3}$$

[1] K. Y. Bliokh, F. J. Rodríguez-Fortuño, F. Nori, and A. V. Zayats, Spin–orbit interactions of light, Nat. Photonics **9**, 796 (2015).
[2] L. Marrucci, E. Karimi, S. Slussarenko, B. Piccirillo, E. Santamato, E. Nagali, and F. Sciarrino, Spin-to-orbital conversion of the angular momentum of light and its classical and quantum applications, J. Opt. **13**, 064001 (2011).
[3] K. Y. Bliokh, A. Aiello, and M. A. Alonso, Spin-orbit interactions of light in isotropic media, in *The Angular Momentum of Light*, edited by D. L. Andrews and M. Babiker (Cambridge University Press, Cambridge, England, 2012), p. 174.
[4] D. Haefner, S. Sukhov, and A. Dogariu, Spin Hall Effect of Light in Spherical Geometry, Phys. Rev. Lett. **102**, 123903 (2009).
[5] C. Schwartz and A. Dogariu, Conservation of angular momentum of light in single scattering, Opt. Express **14**, 8425 (2006).
[6] S. Xiao, J. Wang, F. Liu, S. Zhang, X. Yin, and J. Li, Spin-dependent optics with metasurfaces, Nano. Photonics **6**, 215 (2017).
[7] X. Ling, X. Zhou, X. Yi, W. Shu, Y. Liu, S. Chen, H. Luo, S. Wen, and D. Fan, Giant photonic spin hall effect in momentum space in a structured metamaterial with spatially varying birefringence, Light Sci. Appl. **4**, e290 (2015).
[8] M. Onoda, S. Murakami, and N. Nagaosa, Hall Effect of Light, Phys. Rev. Lett. **93**, 083901 (2004).
[9] P. V. Kapitanova, P. Ginzburg, F. J. Rodríguez-Fortuño, D. S. Filonov, P. M. Voroshilov, P. A. Belov, A. N. Poddubny, Y. S. Kivshar, G. A. Wurtz, and A. V. Zayats, Photonic spin hall effect in hyperbolic metamaterials for polarization-controlled routing of subwavelength modes, Nat. Commun. **5**, 3226 (2014).
[10] D. Gao, R. Shi, A. E. Miroshnichenko, and L. Gao, Enhanced spin hall effect of light in spheres with dual symmetry, Laser Photonics Rev. **12**, 1800130 (2018).
[11] J. E. Hirsch, Spin Hall Effect, Phys. Rev. Lett. **83**, 1834 (1999).
[12] J. Sinova, S. O. Valenzuela, J. Wunderlich, C. H. Back, and T. Jungwirth, Spin hall effects, Rev. Mod. Phys. **87**, 1213 (2015).
[13] K. Yu. Bliokh and Y. P. Bliokh, Conservation of Angular Momentum, Transverse Shift, and Spin Hall Effect in Reflection and Refraction of an Electromagnetic Wave Packet, Phys. Rev. Lett. **96**, 073903 (2006).

[14] R. Shi, D. L. Gao, H. Hu, Y. Q. Wang, and L. Gao, Enhanced broadband spin hall effects by core-shell nanoparticles, Opt. Express **27**, 4808 (2019).
[15] Q. Zhang, D. L. Gao, and L. Gao, Tunable spin hall shift of light from graphene-wrapped spheres, Opt. Express **29**, 9816 (2021).
[16] Y. Q. Wang, H. Hu, Q. Zhang, D. L. Gao, and L. Gao, Topologically-tuned spin hall shift around fano resonance, Opt. Express **28**, 21641 (2020).
[17] J. Soni, S. Mansha, S. D. Gupta, A. Banerjee, and N. Ghosh, Giant Goos-Hänchen shift in scattering: the role of interfering localized plasmon modes, Opt. Lett. **39**, 4100 (2014).
[18] X. Zhou, L. Sheng, and X. Ling, Photonic spin hall effect enabled refractive index sensor using weak measurements, Sci. Rep. **8**, 1221 (2018).
[19] X. Zhou, Z. Xiao, H. Luo, and S. Wen, Experimental observation of the spin hall effect of light on a nanometal film via weak measurements, Phys. Rev. A **85**, 043809 (2012).
[20] S. Chen, X. Ling, W. Shu, H. Luo, and S. Wen, Precision Measurement of the Optical Conductivity of Atomically Thin Crystals via the Photonic Spin Hall Effect, Phys. Rev. Appl. **13**, 014057 (2020).
[21] X. Zhou, X. Ling, H. Luo, and S. Wen, Identifying graphene layers via spin hall effect of light, Appl. Phys. Lett. **101**, 251602 (2012).
[22] R. Wang, J. Zhou, K. Zeng, S. Chen, X. Ling, W. Shu, H. Luo, and S. Wen, Ultrasensitive and real-time detection of chemical reaction rate based on the photonic spin hall effect, APL Photonics **5**, 016105 (2020).
[23] R. Ali, F. A. Pinheiro, F. S. S. Rosa, R. S. Dutra, and P. A. Maia Neto, Optimizing optical tweezing with directional scattering in composite microspheres, Phys. Rev. A **98**, 053804 (2018).
[24] R. Ali, Revisit of generalized kerker's conditions using composite metamaterials, J. Opt. **22**, 085102 (2020).
[25] Y. Gorodetski, K. Y. Bliokh, B. Stein, C. Genet, N. Shitrit, V. Kleiner, E. Hasman, and T. W. Ebbesen, Weak Measurements of Light Chirality with a Plasmonic Slit, Phys. Rev. Lett. **109**, 013901 (2012).
[26] J.-M. Ménard, A. E. Mattacchione, H. M. van Driel, C. Hautmann, and M. Betz, Ultrafast optical imaging of the spin hall effect of light in semiconductors, Phys. Rev. B **82**, 045303 (2010).
[27] K. Y. Bliokh, A. Niv, V. Kleiner, and E. Hasman, Geometrodynamics of spinning light, Nat. Photonics **2**, 748 (2008).
[28] R. P. M. Höller, M. Dulle, S. Thomä, M. Mayer, A. M. Steiner, S. Förster, A. Fery, C. Kuttner, and M. Chanana, Protein-assisted assembly of modular 3d plasmonic raspberry-like core/satellite nanoclusters: Correlation of structure and optical properties, ACS Nano, ACS Nano **10**, 5740 (2016).
[29] M. Inaki, J. Liu, and K. Matsuno, Cell chirality: its origin and roles in left; right asymmetric development, Philosophical Transactions of the Royal Society B: Biological Sciences **371**, 20150403 (2016).
[30] R. Ali, F. A. Pinheiro, R. S. Dutra, F. S. S. Rosa, and P. A. Maia Neto, Enantioselective manipulation of single chiral nanoparticles using optical tweezers, Nanoscale **12**, 5031 (2020).
[31] M. J. Urban, C. Shen, X.-T. Kong, C. Zhu, A. O. Govorov, Q. Wang, M. Hentschel, and N. Liu, Chiral plasmonic nanostructures enabled by bottom-up approaches, Annu. Rev. Phys. Chem. **70**, 275 (2019).
[32] M. Hentschel, M. Schäferling, X. Duan, H. Giessen, and N. Liu, Chiral plasmonics, Sci. Adv. **3**, e1602735 (2017).
[33] X. Duan, S. Yue, and N. Liu, Understanding complex chiral plasmonics, Nanoscale **7**, 17237 (2015).
[34] R. Ali, F. A. Pinheiro, R. S. Dutra, F. S. S. Rosa, and P. A. Maia Neto, Probing the optical chiral response of single nanoparticles with optical tweezers, J. Opt. Soc. Am. B **37**, 2796 (2020).
[35] R. Ali, R. S. Dutra, F. A. Pinheiro, and P. A. Maia Neto, Enantioselection and chiral sorting of single microspheres using optical pulling forces, Opt. Lett. **46**, 1640 (2021).
[36] R. Ali, R. S. Dutra, F. A. Pinheiro, F. S. S. Rosa, and P. A. Maia Neto, Theory of optical tweezing of dielectric microspheres in chiral host media and its applications, Sci. Rep. **10**, 16481 (2020).
[37] O. Hosten and P. Kwiat, Observation of the spin hall effect of light via weak measurements, Science **319**, 787 (2008).
[38] C. F. Bohren and D. R. Huffman, *Absorption and scattering of light by small particles*, in *Absorption and Scattering of Light by Small Particles* (John Wiley and Sons, New York, 1998), Chap. 4, pp. 83–122.
[39] C. F. Bohren and D. R. Huffman, *Absorption and scattering of light by small particles*, in *Absorption and Scattering of Light by Small Particles* (John Wiley and Sons, New York, 1998), Chap. 8, pp. 182–223.
[40] X. Zambrana-Puyalto, X. Vidal, M. L. Juan, and G. Molina-Terriza, Dual and anti-dual modes in dielectric spheres, Opt. Express **21**, 17520 (2013).
[41] A. I. Kuznetsov, A. E. Miroshnichenko, Y. H. Fu, J. Zhang, and B. Luk'yanchuk, Magnetic light, Sci. Rep. **2**, 492 (2012).
[42] R. Ali, Lighting of a monochromatic scatterer with virtual gain, Phys. Scr. **96**, 095501 (2021).
[43] M. Kerker, D.-S. Wang, and C. L. Giles, Electromagnetic scattering by magnetic spheres, J. Opt. Soc. Am. **73**, 765 (1983).
[44] J. H. Poynting, The wave motion of a revolving shaft, and a suggestion as to the angular momentum in a beam of circularly polarised light, Proc. R. Soc. Lond. A **82**, 560 (1909).
[45] Y. Zhao, A. A. E. Saleh, and J. A. Dionne, Enantioselective optical trapping of chiral nanoparticles with plasmonic tweezers, ACS Photonics **3**, 304 (2016).
[46] Y. Shi, T. Zhu, T. Zhang, A. Mazzulla, D. P. Tsai, W. Ding, A. Q. Liu, G. Cipparrone, J. J. Sáenz, and C.-W. Qiu, Chirality-assisted lateral momentum transfer for bidirectional enantioselective separation, Light Sci. Appl. **9**, 62 (2020).
[47] Y. Zhao and J. Dionne, Response to "comment on 'enantioselective optical trapping of chiral nanoparticles with plasmonic tweezers"', ACS Photonics **5**, 2535 (2018).
[48] A. Hayat, J. P. Balthasar Mueller, and F. Capasso, Lateral chirality-sorting optical forces, Proc. Natl. Acad. Sci. **112**, 13190 (2015).
[49] S. B. Wang and C. T. Chan, Lateral optical force on chiral particles near a surface, Nat. Commun. **5**, 3307 (2014).
[50] A. Canaguier-Durand and C. Genet, Plasmonic lateral forces on chiral spheres, J. Opt. **18**, 015007 (2016).
[51] N. Tischler, X. Zambrana-Puyalto, and G. Molina-Terriza, The role of angular momentum in the construction of electromagnetic multipolar fields, Eur. J. Phys. **33**, 1099 (2012).
[52] J. Olmos-Trigo, C. Sanz-Fernández, D. R. Abujetas, A. García-Etxarri, G. Molina-Terriza, J. A. Sánchez-Gil, F. S. Bergeret, and J. J. Sáenz, Role of the absorption on the spin-

orbit interactions of light with si nano-particles, J. Appl. Phys. **126**, 033104 (2019).
[53] K. Y. Bliokh, A. Y. Bekshaev, and F. Nori, Optical Momentum, Spin, and Angular Momentum in Dispersive Media, Phys. Rev. Lett. **119**, 073901 (2017).
[54] S. M. Barnett and M. V. Berry, Superweak momentum transfer near optical vortices, J. Opt. **15**, 125701 (2013).
[55] A. Alù and N. Engheta, How does zero forward-scattering in magnetodielectric nanoparticles comply with the optical theorem? J. Nanophotonics **4**, 041590 (2010).
[56] A. O. Govorov and Z. Fan, Theory of chiral plasmonic nanostructures comprising metal nanocrystals and chiral molecular media, Chem. Phys. Chem. **13**, 2551 (2012).
[57] X. Lan, X. Zhou, L. A. McCarthy, A. O. Govorov, Y. Liu, and S. Link, Dna-enabled chiral gold nanoparticle–chromophore hybrid structure with resonant plasmon–exciton coupling gives unusual and strong circular dichroism, J. Am. Chem. Soc. **141**, 19336 (2019).
[58] C. Ye, J. Jiang, S. Zou, W. Mi, and Y. Xiao, Core–shell three-dimensional perovskite nanocrystals with chiral-induced spin selectivity for room-temperature spin light-emitting diodes, J. Am. Chem. Soc. **144**, 9707 (2022).
[59] A. Guerrero-Martínez, J. L. Alonso-Gómez, B. Auguié, M. M. Cid, and L. M. Liz-Marzán, From individual to collective chirality in metal nanoparticles, Nano Today **6**, 381 (2011).
[60] J. M. Slocik, A. O. Govorov, and R. R. Naik, Plasmonic circular dichroism of peptide-functionalized gold nanoparticles, Nano Lett. **11**, 701 (2011).
[61] M. Raula, D. Maity, Md. H. Rashid, and T. K. Mandal, *In situ* formation of chiral core-shell nanostructures with raspberry-like gold cores and dense organic shells using catechin and their catalytic application, J. Mater. Chem. **22**, 18335 (2012).
[62] S. Lee, K. Sim, S. Y. Moon, J. Choi, Y. Jeon, J.-M. Nam, and S.-J. Park, Controlled assembly of plasmonic nanoparticles: From static to dynamic nanostructures, Adv. Mater. **33**, 2007668 (2021).
[63] L.-A. Wu, W.-E. Li, D.-Z. Lin, and Y.-F. Chen, Three-dimensional sers substrates formed with plasmonic core-satellite nanostructures, Sci. Rep. **7**, 13066 (2017).
[64] F. A. Pinheiro, V. A. Fedotov, N. Papasimakis, and N. I. Zheludev, Spontaneous natural optical activity in disordered media, Phys. Rev. B **95**, 220201(R) (2017).
[65] K. Martens, T. Funck, E. Y. Santiago, A. O. Govorov, S. Burger, and T. Liedl, On the origin of chirality in plasmonic meta-molecules, ACS Nano **16**, 16143 (2022).
[66] G. Zheng, J. He, V. Kumar, S. Wang, I. Pastoriza-Santos, J. Pérez-Juste, L. M. Liz-Marzán, and K.-Y. Wong, Discrete metal nanoparticles with plasmonic chirality, Chem. Soc. Rev. **50**, 3738 (2021).
[67] F. Graf, J. Feis, X. Garcia-Santiago, M. Wegener, C. Rockstuhl, and I. Fernandez-Corbaton, Achiral, helicity preserving, and resonant structures for enhanced sensing of chiral molecules, ACS Photonics **6**, 482 (2019).
[68] Q. Zhang, J. Li, and X. Liu, Optical lateral forces and torques induced by chiral surface-plasmon-polaritons and their potential applications in recognition and separation of chiral enantiomers, Phys. Chem. Chem. Phys. **21**, 1308 (2019).

Correction: The omission of an Acknowledgments section and conflict of interest statement have been fixed.